Adjoint-Based Design of a Distributed Propulsion Concept with a Power Objective

Irian Ordaz*, Eric J. Nielsen†, Sriram K. Rallabhandi‡
NASA Langley Research Center, Hampton, VA 23681
and
Boris Diskin§
National Institute of Aerospace, Hampton, VA 23666

The adjoint-based design capability in FUN3D is extended to allow efficient gradient-based optimization and design of concepts with highly integrated and distributed aero-propulsive systems. Calculations of propulsive power, along with the derivatives needed to perform adjoint-based design, have been implemented in FUN3D. The design capability is demonstrated by the shape optimization and propulsor sizing of NASA's PEGASUS aircraft concept. The optimization objective is the minimization of flow power at the aerodynamic interface planes for the wing-mounted propulsors, as well as the tail-cone boundary layer ingestion propulsor, subject to vehicle performance and propulsive constraints.

I. Introduction

The aerospace industry continues to invest in research and novel technologies that promise improvements in aircraft efficiency, which can be characterized as an indicator of fuel burn or alternative energy consumption. A reduction in fuel burn, particularly during the cruise segment, results in a reduction of harmful emissions, and potentially lower operational costs.

Past research conducted to improve aircraft efficiency has focused on technologies that are applicable to the main wing such as winglets, which provide a reduction in lift-induced drag. There is currently growing interest in technologies that take advantage of the complex interaction between the vehicle aerodynamics and the propulsion system in order to increase fuel efficiency. Two technologies of particular interest that leverage aero-propulsive interactions to improve aircraft efficiency are boundary layer ingestion (BLI) and distributed electric propulsion (DEP). BLI takes advantage of the low momentum flow from an ingested boundary layer (BL) to reduce engine ram drag and, thus, the power required to produce thrust. DEP is a highly scalable solution which allows greater design authority due to the closer coupling of the aerodynamic and propulsion systems.

Examples of recent aircraft concepts that make use of one or both of these technologies include NASA's Single-aisle Turboelectric Aircraft with an Aft Boundary Layer Propulsor (STARC-ABL) [1], X-57 Maxwell [2], and Parallel Electric-Gas Architecture with Synergistic Utilization Scheme (PEGASUS) [3]. These highly integrated aero-propulsive systems, however, bring a new set of modeling and analysis challenges. The more complex multidisciplinary problem requires closer coupling between the aerodynamic and propulsion disciplines than in the past. This requires a paradigm shift for disciplines that have traditionally operated to some extent independently of each other with rigid interfaces for transferring data between them.

Gray, Kenway, Mader, and Martins [4] demonstrated the use of an adjoint method to minimize the shaft power required for the tail-cone thruster of NASA's STARC-ABL BLI propulsor. The discrete adjoint implementation that is presented in this paper is similar to their earlier work. However, we are also interested in understanding not only the propulsive scaling, and power and thrust split between different propulsors, but also the optimization of the propulsor installment on the vehicle by providing design sensitivities with respect to position and orientation of the propulsors.

This work targets concepts with highly distributed propulsion such as PEGASUS and X-57. Note that design sensitivities with respect to the propulsion model are not yet implemented. Future work will couple the propulsion model and their respective design sensitivities. A subset of our current implementation is applied to the PEGASUS concept, a parallel hybrid electric concept with strategically positioned propulsors, to optimize the outer-mold-line

*Aerospace Engineer, Aeronautics Systems Analysis Branch, AIAA Member.
†Research Scientist, Computational AeroSciences Branch, AIAA Associate Fellow.
‡Aerospace Engineer, Aeronautics Systems Analysis Branch, AIAA Associate Fellow.
§NIA Research Fellow, AIAA Associate Fellow.

(OML) and determine the optimal size and power requirements for wing-mounted and tail-cone propulsors. A rendered image of the PEGASUS concept is shown in Fig. 1.

The paper is organized into six sections. Following this introduction, Section II describes the FUN3D solver. Section III describes the actuator disk model representing the aero-propulsive interface. Section IV discusses the optimization formulation, including the objective function, constraints, discrete adjoint formulation for the flow power objective at the aero-propulsive interface, and verification of the sensitivity analysis. Section V provides a demonstration of the optimization capability with two simplified cases using a body of revolution, and with the more relevant PEGASUS concept. Finally, a summary of the work, as well as future work is presented in Section VI.

Fig. 1 PEGASUS concept (Source: Ref. 3).

II. FUN3D Solver

Aerodynamic solutions and adjoint-based sensitivities are computed using FUN3D [5, 6]. FUN3D is a finite-volume node-centered unstructured-grid CFD solver for Reynolds-Averaged Navier-Stokes (RANS) equations, which is widely used for high-fidelity analysis and adjoint-based design of complex flows. FUN3D solves the Navier-Stokes equations on mixed-element grids containing arbitrary combinations of tetrahedra, pyramids, prisms, and hexahedra. Dual control volumes are constructed around nodes by connecting centers of grid elements, centers of element faces, and edge medians. At each control-volume face, the inviscid flux is computed using Roe's flux-difference splitting Riemann solver. For second-order accuracy, solution values at the face are obtained using a monotonic upstream scheme for conservation laws (MUSCL) [7], with unweighted least-squares gradients computed at the grid points. The viscous fluxes use the full viscous stress tensors. For tetrahedral meshes, the viscous fluxes are discretized using the Green–Gauss element-based gradients; this formulation is equivalent to a Galerkin-type approximation. For non-tetrahedral elements, the Green–Gauss gradients are augmented with edge-based terms. Turbulence is computed using the one-equation model of Spalart-Allmaras [8].

III. Actuator Disk Model

The actuator disk model used in the current work is based on the formulation originally outlined by Ref. 9. In this approach, a force vector distributed over an auxiliary two-dimensional disk grid is applied as a source term in the governing equations to model the approximate effect of a rotor imparting an external force on the fluid.

In the original implementation described in Ref. 9, the force vector from each location in the auxiliary grid augments the residual equations at the nearest grid point in the three-dimensional mesh used to represent the fluid solution. This implementation is not suitable for sensitivity analysis of the fluid solutions with respect to rotor disk coordinates. The relationships between the force locations on the disk and the corresponding nearest fluid-grid points are piecewise constant. Infinitesimal deviations in a force location do not change the nearest grid point and therefore do not affect the flowfield. Thus, the sensitivity of fluid solutions with respect to the disk coordinates are identically zero.

The formulation is modified to provide a continuous dependence between the rotor disk coordinates and the force representation on the fluid grid. The force vector defined at a location in the rotor disk is distributed between vertices of the surrounding tetrahedral element of the fluid grid. The specific weights assigned to each vertex are based on the convex linear interpolation within the tetrahedral element to the force location. If the surrounding element is not

tetrahedral, four vertices of this element, which form a tetrahedral sub-element surrounding the force location, are identified and used for the force distribution. In this manner, any deviation in the location of the disk grid produces a continuous change in the force distribution and in the solution of the governing equations.

IV. Optimization Formulation

A. Objective Function

The objective function to be minimized is based on the flow power required to maintain a prescribed vehicle performance. The power is evaluated over all actuator disks by integrating the inner product of the distributed actuator disk force vector with the local velocity vector. The local velocity vector is interpolated to the actuator disk in a procedure that is reciprocal to the weighted element-based force distribution approach described in Section III. A surrounding tetrahedral element is identified for each force location at an actuator disk grid point and used to linearly interpolate the local velocity vectors to the force location. The objective function, $\mathcal{F}$, shown in Eq. 1 represents the flow power, $\mathcal{P}$.

$$\mathcal{F}(\boldsymbol{D},\boldsymbol{X},\boldsymbol{Q}) = \mathcal{P} = \int_A \boldsymbol{T}\cdot\boldsymbol{v}\,dA \tag{1}$$

which depends on design parameters, $\boldsymbol{D}$; computational grid, $\boldsymbol{X}$; and solution, $\boldsymbol{Q}$. Here, the thrust is denoted by $\boldsymbol{T}$ and the product $\boldsymbol{T}\cdot\boldsymbol{v}$ is integrated over the aerodynamic interface plane (AIP) of the propulsors with area, A. Design parameters, $\boldsymbol{D}$, include the angle-of-attack, α, the actuator tip radius, R_{tip} (or diameter, D), the tip speed ratio, λ, the coefficient of thrust, C_T, the actuator center position, $\boldsymbol{x} = [x_0, y_0, z_0]$, the thrust vector angles, $\boldsymbol{\phi} = [\phi_1, \phi_2, \phi_3]$, and shape variables on the OML. Note that, for the demonstration cases in Section V, only a subset of the available actuator design variables in $\boldsymbol{D}$ will be used depending on the application.

The relation between thrust and our design variables is given in Eq. 2 and 3, where V_a is the speed of advance, n represents the revolutions per second, and D, the diameter of the actuator disk (or $2R_{tip}$). Not that not all design variables will

$$T = \rho n^2 D^4 K_T, \text{ where: } K_T = \frac{\pi^3 C_T}{4} \tag{2}$$

$$\lambda = \frac{\pi n D}{V_a} \tag{3}$$

B. Performance Constraints

Performance constraints must be placed on the net force acting on the vehicle to prevent the optimizer from driving thrust, $\boldsymbol{T}$, to zero. This is because thrust, which is used to calculate the power objective, is directly related to our design variables, as was shown previously.

A diagram of the forces acting on the aircraft with a flight path angle of zero degrees is shown in Fig. 2, and the corresponding force equations are given in Eq. 4. The lift, drag, weight, and thrust vectors are denoted by L, D, W, and T, respectively. These equations are normalized by dynamic pressure, q, and reference area, S, as shown in Eq. 5. The thrust pitch angle is given by ϕ_2 which is 0 deg along the z-axis and -90 deg along the x-axis. For all optimization cases presented in Section V, the thrust vector denoted by $\boldsymbol{\phi}$ is held constant and it is chosen to be parallel to the x-axis ($\phi_2 = -90$ deg). Also note that C_T^* is the dimensional rotor thrust normalized by qS, and it can also be expressed in terms of the rotor thrust coefficient by Eq. 6.

$$\begin{aligned} F_x &= -L\sin\alpha + D\cos\alpha + W\sin\alpha + \sum_{i=1}^{n_{\text{prop}}} T_i \sin\phi_{2,i} \\ F_z &= L\cos\alpha + D\sin\alpha - W\cos\alpha + \sum_{i=1}^{n_{\text{prop}}} T_i \cos\phi_{2,i} \end{aligned} \tag{4}$$

$$C_x = -C_L \sin\alpha + C_D \cos\alpha + C_W \sin\alpha + \sum_{i=1}^{n_{\text{prop}}} C_{T_i}^* \sin\phi_{2,i}$$
$$C_z = C_L \cos\alpha + C_D \sin\alpha - C_W \cos\alpha + \sum_{i=1}^{n_{\text{prop}}} C_{T_i}^* \cos\phi_{2,i} \tag{5}$$

$$C_T^* = \frac{\pi\lambda^2 D^2}{2S} C_T \tag{6}$$

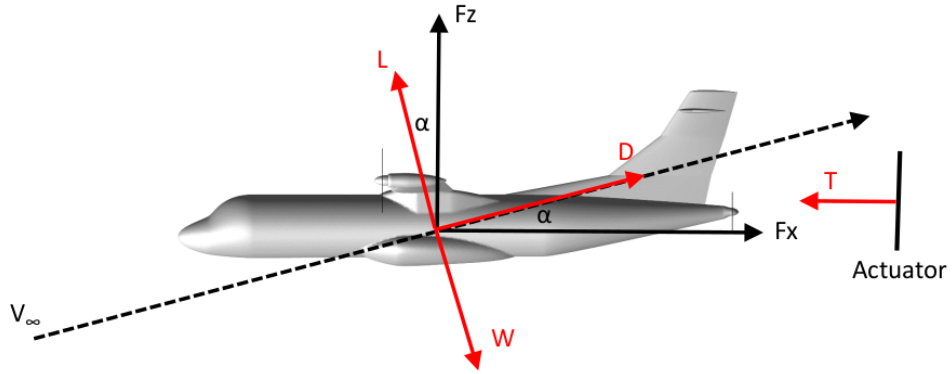

Fig. 2 Summation of forces.

C. Propulsor Constraints

Additional constraints are placed on the actuator disk model in the absence of detailed characteristics and performance models for the propulsion system. The constraints ensure that the performance is realistic and representative for a propulsive system. These are enforced by careful selection of the design variable bounds for rotor coefficient of thrust, C_T, tip speed ratio, λ, rotational speed, n, and diameter, D. The Mach number at the tip of the rotor is constrained by a maximum Mach number, M_{tip}. This constraint is imposed by an upper limit on λ, as given by Eq. 7. For simplicity, Eq. 7 assumes that the speed of advance, V_a, is approximately equal to the freestream velocity, V_∞, and that the local speed of sound at the rotor tip is approximately equal to the freestream speed of sound.

$$\lambda = \frac{\pi n D}{V_a} \approx \frac{\pi n D}{V_\infty} \leq \sqrt{\left(\frac{M_{tip}}{M_\infty}\right)^2 - 1} \tag{7}$$

For the demonstration cases in Section V, the maximum disk loading (T/A) and rotational speed, n, are 50 lb/ft^2 and 2,500 RPM, respectively, based on historical observations for the PEGASUS class of aircraft. Also, λ is less than or equal to 1.37, in order to ensure that M_{tip} is always less than 0.85.

The thrust equation defined in Eq. 2 can be re-written in terms of λ, as shown in Eq. 8. Knowing the limit on disk loading and λ, we can calculate a maximum value for the C_T, as shown in Eq. 9. For simplicity, we round up the maximum value of C_T to 0.08, which corresponds to a disk loading value of approximately 51 lb/ft^2. Knowing the maximum values of λ and n, it is also possible to calculate the maximum diameter of the actuator by solving Eq. 7 for the diameter, D.

$$\frac{T}{A} = \rho C_T \pi^2 n^2 D^2 = \rho V_\infty^2 C_T \lambda^2 \leq 50 \tag{8}$$

$$C_T \leq \frac{\left(\frac{T}{A}\right)_{max}}{\rho V_\infty^2 \lambda_{max}^2} = 0.0783 \tag{9}$$

D. Adjoint Formulation

The discrete adjoint formulation for flow and grid equations is described in Ref. 6. The implementation relies on the comprehensive and verified sensitivity analysis for steady and unsteady flows computed on general static and dynamic, rigidly moving and deforming, single-block and overset grids [6, 10]. The optimization problem can then be formulated as follows

$$\text{Find: } \min_{\boldsymbol{D}} \mathcal{F}(\boldsymbol{D},\boldsymbol{X},\boldsymbol{Q}), \quad \text{subject to } \boldsymbol{R}(\boldsymbol{D},\boldsymbol{X},\boldsymbol{Q}) = 0 \text{ and } \boldsymbol{G}(\boldsymbol{D},\boldsymbol{X}) = 0 \tag{10}$$

Here, $\boldsymbol{R}(\boldsymbol{D},\boldsymbol{X},\boldsymbol{Q})$ is the discrete residual vector of the flow equations, including a source term for the actuators disks, that depends on the design variables, grid coordinates, and flow solution; $\boldsymbol{G}(\boldsymbol{D},\boldsymbol{X})$ is the residual vector of the grid equations that depends on the design variables and grid coordinates. The grid equations are based on the linear elasticity equations of solid mechanics as described in Refs. 11 and 12.

A Lagrangian is formed to compute the sensitivity of the objective function, $\mathcal{F}$, to the design parameters,

$$\mathcal{L} = \mathcal{F}(\boldsymbol{D},\boldsymbol{X},\boldsymbol{Q}) + \boldsymbol{\Lambda}_R^T \boldsymbol{R}(\boldsymbol{D},\boldsymbol{X},\boldsymbol{Q}) + \boldsymbol{\Lambda}_G^T \boldsymbol{G}(\boldsymbol{D},\boldsymbol{X}) \tag{11}$$

Here, $\boldsymbol{\Lambda}_R$ is a vector of Lagrange multipliers corresponding to the flow equations and $\boldsymbol{\Lambda}_G$ is a vector of Lagrange multipliers corresponding to the grid equations. The Lagrangian is differentiated with respect to the design parameters,

$$\frac{d\mathcal{L}}{d\boldsymbol{D}} = \frac{\partial \mathcal{F}}{\partial \boldsymbol{D}} + \boldsymbol{\Lambda}_R^T \frac{\partial \boldsymbol{R}}{\partial \boldsymbol{D}} + \boldsymbol{\Lambda}_G^T \frac{\partial \boldsymbol{G}}{\partial \boldsymbol{D}} + \left\{ \frac{\partial \mathcal{F}}{\partial \boldsymbol{X}} + \boldsymbol{\Lambda}_R^T \frac{\partial \boldsymbol{R}}{\partial \boldsymbol{X}} + \boldsymbol{\Lambda}_G^T \frac{\partial \boldsymbol{G}}{\partial \boldsymbol{X}} \right\} \frac{d\boldsymbol{X}}{d\boldsymbol{D}} + \left\{ \frac{\partial \mathcal{F}}{\partial \boldsymbol{Q}} + \boldsymbol{\Lambda}_R^T \frac{\partial \boldsymbol{R}}{\partial \boldsymbol{Q}} \right\} \frac{d\boldsymbol{Q}}{d\boldsymbol{D}} \tag{12}$$

Equating the coefficients of $\frac{d\boldsymbol{X}}{d\boldsymbol{D}}$ and $\frac{d\boldsymbol{Q}}{d\boldsymbol{D}}$ to zero results in a set of adjoint equations for $\boldsymbol{\Lambda}_R$ and $\boldsymbol{\Lambda}_G$

$$\frac{\partial \mathcal{F}}{\partial \boldsymbol{Q}} + \boldsymbol{\Lambda}_R^T \frac{\partial \boldsymbol{R}}{\partial \boldsymbol{Q}} = 0 \tag{13}$$

$$\frac{\partial \mathcal{F}}{\partial \boldsymbol{X}} + \boldsymbol{\Lambda}_R^T \frac{\partial \boldsymbol{R}}{\partial \boldsymbol{X}} + \boldsymbol{\Lambda}_G^T \frac{\partial \boldsymbol{G}}{\partial \boldsymbol{X}} = 0 \tag{14}$$

With Lagrange multipliers satisfying Eqs. 13 and 14, the sensitivity of the objective function with respect to the design variables is computed as

$$\frac{d\mathcal{L}}{d\boldsymbol{D}} = \frac{d\mathcal{F}}{d\boldsymbol{D}} = \frac{\partial \mathcal{F}}{\partial \boldsymbol{D}} + \boldsymbol{\Lambda}_R^T \frac{\partial \boldsymbol{R}}{\partial \boldsymbol{D}} + \boldsymbol{\Lambda}_G^T \frac{\partial \boldsymbol{G}}{\partial \boldsymbol{D}} \tag{15}$$

In this manner, sensitivities of an objective function with respect to an arbitrary number of design parameters may be computed at a cost equivalent to that of one analysis. Note that in Eq. 14, the flow equations, $\boldsymbol{R}$, and grid equations, $\boldsymbol{G}$, need to be differentiated with respect to the propulsive design variables, $\boldsymbol{D}$. We also need to calculate the derivatives for the objective function ($\frac{\partial \mathcal{F}}{\partial \boldsymbol{D}}$, $\frac{\partial \mathcal{F}}{\partial \boldsymbol{X}}$, $\frac{\partial \mathcal{F}}{\partial \boldsymbol{Q}}$).

E. Consistency of Linearization

To determine the discrete consistency of the adjoint implementation, sensitivity derivatives are verified using an independent approach based on complex variables [Refs. 13–15]. Unlike traditional finite-difference derivative approximations based on real-valued perturbations, the complex-variable form of the finite-difference analysis is free of subtraction errors and can be used to verify a manual implementation of an adjoint-based sensitivity analysis.

Sensitivity derivatives are computed for a fully turbulent flow over the simple configuration shown in Fig. 3(b), with a single actuator disk placed in close proximity to a body of revolution. For these comparisons, the magnitude of the imaginary perturbation is chosen to be $1\text{x}10^{-50}$ and all equation sets are solved to machine precision. Tables A-1 through A-3 of Appendix A show sensitivity derivatives of the power-based objective function and the two force constraints with respect to α, a shape parameter used to specify the body geometry, and several input parameters required by the actuator disk model. The agreement between the results obtained using the discrete adjoint approach and those of the complex-variable implementation is excellent.

V. Demonstration Cases

This section contains three demonstration cases of increasing complexity intended to assess the new design implementation. All cases are analyzed at a Mach number of 0.5 and altitude of 20,000 ft. The grids are fully tetrahedral and a y^+ of 1.0 is used for the BL initial grid spacing. Currently, the actuator model used here does not include the effects of torque and swirl. Therefore, any potential benefit or losses associated with swirl effects are not modeled and could affect the results presented in this study.

A. Optimization of Actuator Position for BLI Application

The first case studied is that of a body of revolution at an α of zero degrees with an actuator placed near the trailing edge acting as a BLI propulsor. The unconstrained optimization problem is given in Eq. 16, where $\boldsymbol{D}$, is the z-location of the actuator. The body of revolution, which is shown in Fig. 3(b), has a length of 12 inches and a fineness ratio of 10. The CFD grid consists of 1.05 million nodes and 6.3 million tetrahedral elements.

$$\text{Find: } \min_{\boldsymbol{D}} \mathcal{F} = \mathcal{P}^2 \tag{16}$$

The optimizer convergence history (raw function evaluations) for the power objective and z-location design variable is shown in Fig. 3(a). The top image in Fig. 3(b) shows the baseline actuator (denoted by the vertical black line) at a z-location of -1.5 inches, which is one radius distance below the chord line of the body of revolution. As expected, in an attempt to minimize the inflow velocity (and flow power), the optimizer translated the actuator in the $+z$-direction to place it just behind the body of revolution. The optimized actuator location ($z = -0.015$ inches) is shown in the bottom image in Fig. 3(b).

In theory, the optimal position of the actuator is directly behind the body of revolution at $z = 0$. However in practice, the flow solution around the geometry is not exactly symmetric due to the grid itself being non-symmetric (we model the full grid with no symmetry imposed). This grid-induced asymmetry can be observed in the wake flow region for the *theoretically* symmetric cases shown in Fig. 5. Nonetheless, this case demonstrates the capability to optimize the location of propulsors. Despite its simplicity, this capability is useful for the optimization of concepts with highly distributed propulsion, where the ideal position of a propulsor is not obvious.

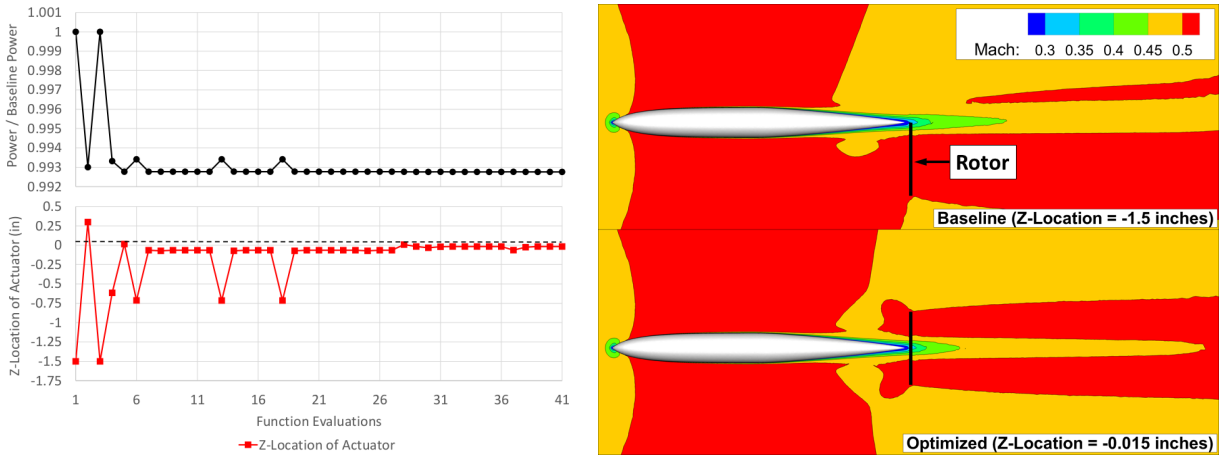

(a) Convergence history

(b) Comparison of flow solutions

Fig. 3 Optimization of actuator position under BLI conditions.

B. Optimization of Actuator Radius for BLI Application

The second optimization case uses the same body of revolution presented earlier. However, for this case, we try to find the optimum actuator size for a BLI application. The actuator is once again placed near the trailing edge of the geometry and centered about the mid-chord line of the body.

The objective function for this optimization problem is the same as in the previous case (Eq. 16) but a force constraint along the x-direction is now added (Eq. 17). In this case, $\boldsymbol{D}$, is the actuator radius. Two different optimizations are

conducted starting with one actuator that is undersized and another one that is oversized. The actuator is undersized when it produces less thrust than necessary to balance the force along the x-direction, and an oversized actuator exhibits the opposite behavior.

$$C_x^2 \leq \varepsilon \tag{17}$$

The force is constrained along the axial (x) direction to ensure that the tolerance (ε) on the net force is less than or equal to 1% of the total drag force. As described in Section IV-C, this constraint is required to ensure that the optimizer does not simply drive the thrust to *zero* in an effort to minimize power.

A radius of 0.12 inches and 1.5 inches was chosen for the undersized and oversized actuators, respectively. The convergence of the radius design variable for both optimization cases is shown in Fig. 4. The results show that both cases successfully converge to the same optimum radius of 0.54 inches. The design history of flow power relative to baseline power in Fig. 4 shows how the undersized and oversized rotors have to scale up and down to produce more and less thrust, respectively. The scaling is driven by the net force constraint along the axial direction.

A comparison of the flow solution for the undersized and oversized rotors is shown at the top of Fig. 5(a) and 5(b), respectively. Their corresponding optimized flow solutions are shown directly below the baseline flow solutions and the actuators are once again denoted by the vertical black line positioned directly behind the body.

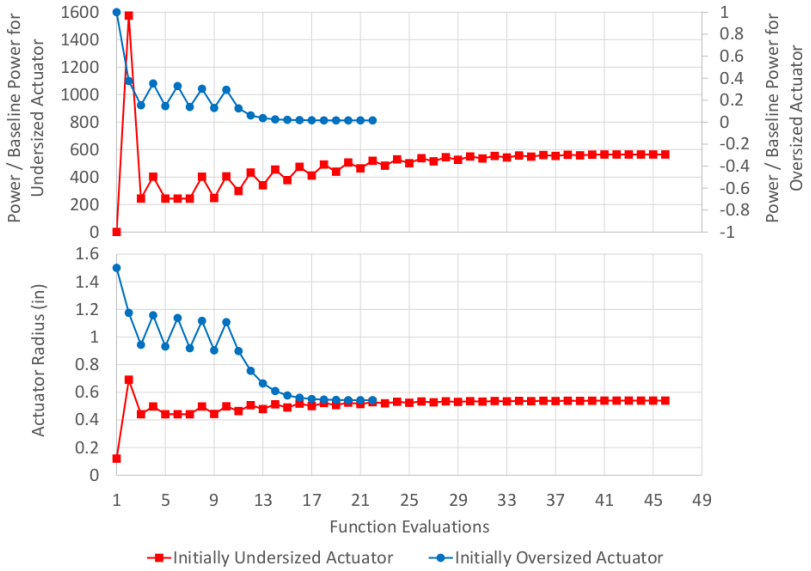

Fig. 4 Convergence history for the optimization of actuator radius.

C. Optimization of PEGASUS Concept

The implemented optimization capability is demonstrated using the PEGASUS hybrid electric regional aircraft concept. This concept, shown in Fig. 1, is based on the ATR-42-500 aircraft and consists of two parallel hybrid electric propulsors located at the wing tips and electric propulsors located mid-wing and at the fuselage tail-cone. For simplicity, the mid-wing propulsors are omitted and only the tip rotors and tail-cone BLI rotor are used for the demonstration case. Note however, that the implementation does not restrict the number of actuator disks that can be used for optimization. The flight condition for this demonstration case is once again cruise at an altitude of 20,000 ft, a Mach number of 0.5, and a vehicle weight of 35,000 lb. This cruise condition requires a coefficient of lift (C_L) of 0.351 based on a reference area (S) of 586 ft^2, and a dynamic pressure of 170.1 lb/ft^2. The CFD grid consists of 10.8 million nodes and 64.9 million tetrahedral elements.

1. Problem Definition

The optimization problem described in Eq. 18 seeks to minimize the total flow power (or propulsor power requirement) from the wing-mounted and tail-cone propulsors (a total of $n_{\text{prop}} = 3$ equally weighted propulsors). Constraints are

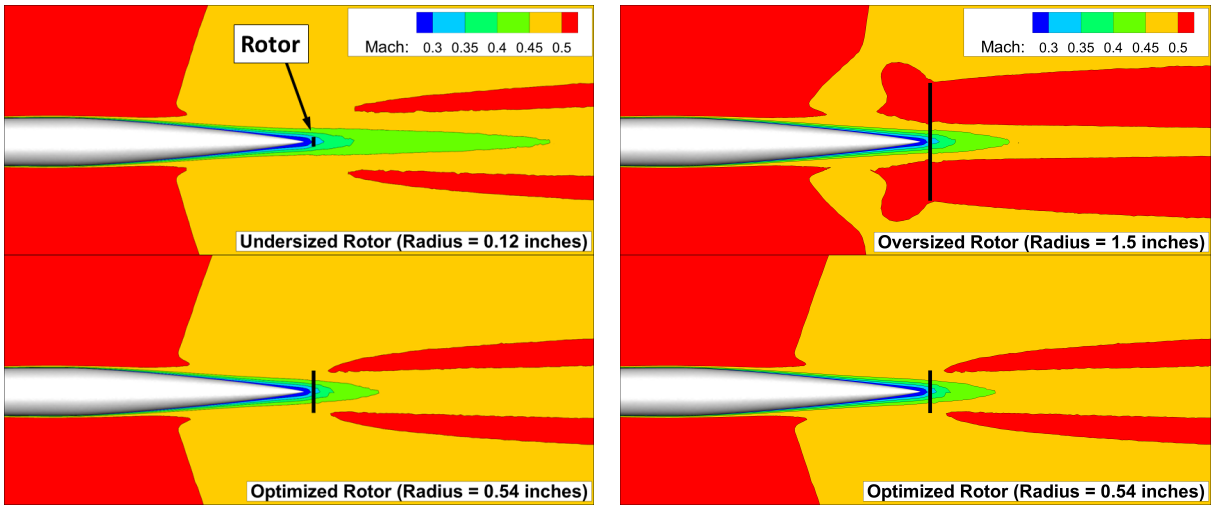

(a) Initially undersized rotor

(b) Initially oversized rotor

Fig. 5 Comparison of flow solution for the optimization of the undersized and oversized actuator disks.

placed on the geometric shape variables for the wing and fuselage, on the propulsors-specific variables for the wing-tip and tail-cone BLI rotors, and on the net force (F_x and F_z), which is required to be within 200 lb of the required net force to maintain steady and level flight in cruise. Additional implicit constraints are placed on maximum rotor tip Mach number (limited to Mach of 0.85), a maximum disk loading of 50 lb/ft^2, and a maximum rotor diameter based on a maximum rotational speed of 2,500 RPM, as described in Section IV-C.

$$\begin{aligned} &\text{Find: } \min_{\boldsymbol{D}} \mathcal{F} = \sum_{i=1}^{n_{\text{prop}}} \omega_i \mathcal{P}_i^2 \\ &\text{Subject to:} \\ &\qquad C_x \leq 0 \\ &-\varepsilon \leq C_z \leq \varepsilon \end{aligned} \tag{18}$$

2. Geometry Parameterization

The surface mesh for the aircraft is parameterized using a free-form shape deformation tool called BandAIDS [16]. BandAIDS is designed for use with general surface topologies and provides a set of design variables describing general displacements normal to the underlying surface.

The aft fuselage patch is split into 20 sections, with each section containing 10 NURBS control points to change the underlying shape using BandAIDS. To force symmetry, control points on one side of the fuselage are linked with their identical counterpart points across the plane of symmetry. This reduces the number of variables in half to 100. For the first 15 sections, only three linked variables are allowed to vary to ensure that the vertical tail intersection with the fuselage is not altered; this accounts for 45 design variables. Of the remaining 5 sections, the first four sections are allowed to vary with a symmetry constraint via variable linking, while the last section is not allowed to vary, ensuring C0 continuity of the deformed surfaces. This scheme results in 20 variables in the last five sections making the total 65 active design variables on the aft fuselage. Figure 6 depicts the locations on the geometry that are parameterized for shape optimization. The primary criterion for the choice of these locations is potential impact on the BLI propulsor.

In addition to the above OML shape variables, there are 3 variables that are allowed to vary for each of the tail-cone and wing-tip rotors, namely a) thrust coefficient, b) tip speed ratio and c) diameter. However to maintain symmetry, the wing-tip rotor variables corresponding to either side of the symmetry plane are linked together to vary as a single variable. This increases the number of independent design variables by 6. Finally, including α as an independent variable makes the total number of design variables used by the optimizer to be 72.

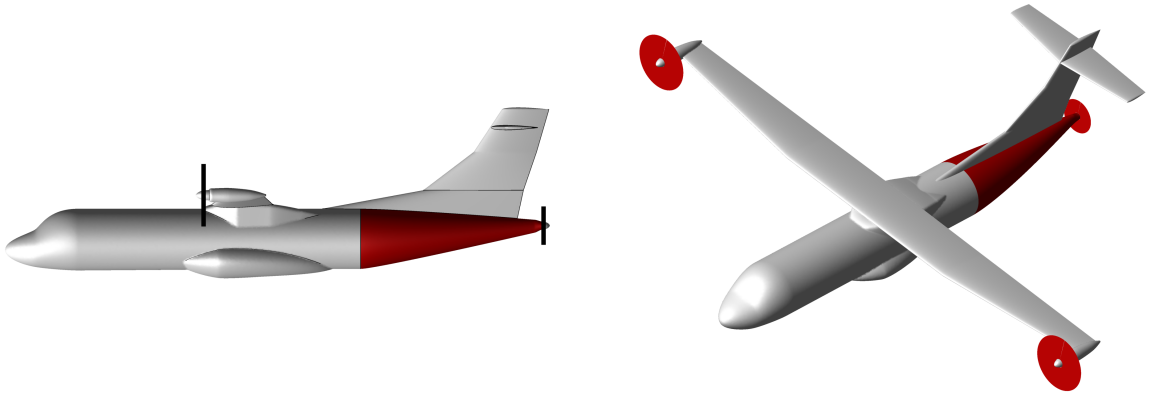

Fig. 6 Locations parameterized for shape optimization.

3. Discussion of Optimization Results

The optimization was conducted on 2,000 cores of Intel Skylake processors, dual-socket 20-core Xeon Gold 6148 model with a base clock speed of 2.4 GHz. The FUN3D flow solver and the adjoint solver with one objective and two constraints require 6.3 and 10.4 minutes, respectively. A complete design with 16 design cycles requires just under 5 wall-clock hours.

A history of the objective function evaluations as well as net force along the x- and z-directions for PEGASUS concepts is given in Fig. 7. The optimizer converges very quickly close to its optimum within the first few design evaluations. Note that data points in Fig. 7 are raw function evaluations, and some constraint evaluations are infeasible steps by the optimizer. These graphs include red dash lines denoting the constraint on net force in the x-direction, and blue dash lines denoting the net force constraint in the z-direction. The optimizer also finds this feasible region of the design space within the first few design evaluations. The force constraint along the x-direction is relatively stable and remains feasible through most of the optimization, while the force constraint along the z-direction tends to exhibit more excursions into the infeasible space due to the high sensitivity of the force along this direction to α.

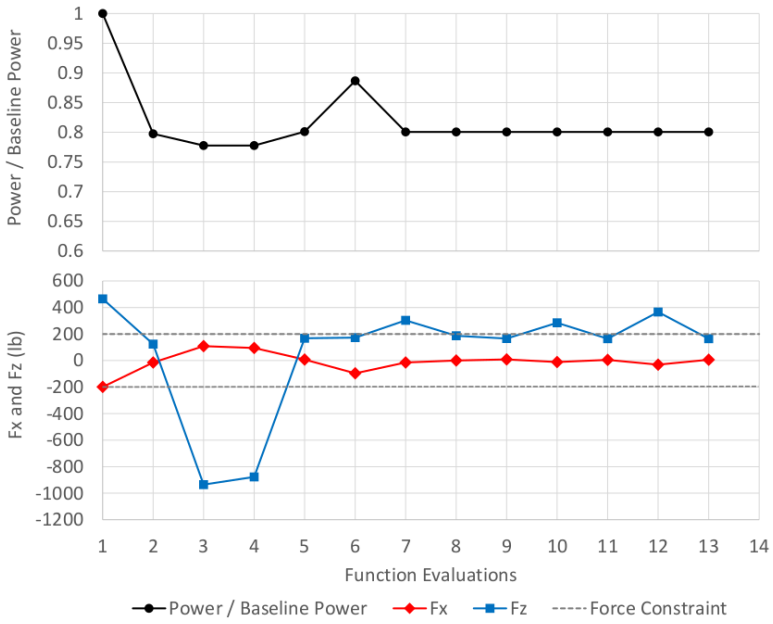

Fig. 7 Design history of objective and performance constraints.

This optimistic result is meant to be demonstrative of the optimization capability and should be considered only as an academic exercise; the actuator design variable bounds have relatively relaxed constraints for tip Mach number

(M_{tip} = 0.85), and propeller rotational speed (n = 2,500 RPM), and are not representative of an existing propulsion system. Furthermore, there are also physical phenomena associated with the actuator disk that are not being modeled. The actuator model that is currently implemented has a constant thrust loading and does not model the swirl effect associated with the torque imparted by the propulsor on the flow. A swirl effect will result in efficiency losses but may also provide a reduction in induced drag which would in turn reduce the propulsive power requirement. As a result, the model of the tip rotors produce no reduction in induced drag. In the current formulation there is also no way to capture efficiency losses associated with the flow distortion for the BLI propulsor, and there is no consideration for the varying scaling effects of different types of propulsors and energy sources since we do not have sensitivities with respect to the propulsion system. In the absence of propulsion sensitivities, we minimize total power as a surrogate for fuel or energy consumption.

A comparison of the propulsive design variables for the baseline and final design of the PEGASUS concept are provided in Table 1. These results show that the optimizer is exploiting the power saving benefit of the BLI propulsor. The BLI propulsor increases in size from a radius of 2.66 ft to 2.87 ft but this is limited by the implicit constraint on rotor tip Mach number of 0.85. The C_T on the BLI propulsor is maximized to the upper bound of 0.08 which corresponds to a disk loading of approximately 51 lb/ft^2, and rotational speed remains relatively unchanged. Recall that the maximum disk loading in Table 1 is greater than 50 lb/ft^2 because maximum C_T was rounded up to 0.08. Also note that this rotor would require further design considerations regarding tail scrape angle during takeoff which are not considered in this work. Meanwhile, the tip rotor trades size for increased rotational speed; its radius decreases from 4.3 ft to 4.0 ft (lower bound of the radius), while its rotational speed increases slightly from 1,439 RPM to 1,542 RPM.

Table 1 Comparison of propulsive design variables

	C_T	λ	R_{tip} (ft)	n (RPM)	M_{tip}	Thrust (lb)	A (ft^2)	Disk loading (lb/ft^2)
Baseline (BLI rotor)	0.077	1.251	2.66	2,326	0.80	912	22.2	41.1
Optimized (BLI rotor)	0.080	1.370	2.87	2,361	0.85	1,323	25.9	51.1
Baseline (wing tip rotor)	0.029	1.251	4.3	1,439	0.80	912	58.1	15.7
Optimized (wing tip rotor)	0.026	1.247	4.0	1,542	0.80	692	50.3	13.7

A comparison of Mach contours for the baseline and optimized design is provided in Fig. 8. The vertical lines in the wake region are markers which are placed every 2 ft, starting at 78 ft and ending at 100 ft. This can be used to visualize the wake filling effect of the BLI propulsor, as the low Mach number contours for the optimized concept recover to freestream quicker than the baseline. Despite the significant change in magnitude of the flow velocities in the wake, the shape of the wake is not significantly altered due to the uniform disk loading currently used.

The contours of the wake produced by the horizontal tail also show the effect of the small increase in α from 3.2-deg of the baseline to 3.28-deg of the optimized concept. In fact, despite the reduction in power, the coefficient of drag was found to increase from 0.0256 to 0.0272, equivalent to a 6.2% increase in drag. This increase was found to be mainly due to an increase in drag of 21% over the parameterized aft fuselage region shown in Fig. 6, a direct result of the aerodynamic interaction between the airframe and the propulsor.

The optimized thrust split between the two wing mounted propulsors and the tail propulsor was observed to be 53/47, meaning 53% of the thrust is produced by the two wing mounted propulsors and 47% is produced by the tail propulsor. Recall, that the initial design produced equal thrust from each of the three propulsors, which corresponds to a 66/33 split. In contrast, the optimized power split between the two wing mounted rotors and the tail propulsor was observed to vary from 86/14 to 70/30 for the optimized configuration, placing higher power requirements on the tail propulsor. This will be strongly limited by the type of propulsive system and energy source that is used and will require addressing some of the modeling concerns described earlier. A tail propulsor that scales poorly to this power requirement may result in a significant increase in weight, which would introduce a drag penalty, and place greater power requirements on the main wing propulsor if the tail propulsor is not able to meet the demand. Nonetheless, the optimization exhibits the design trends that would be expected based on the physics being modeled.

A plot of the magnitude of the displacement along the OML of the parameterized aft fuselage region is shown in Fig. 9. Although, the sensitivity of power with respect to actuator design variables is significantly larger than the sensitivity to OML shape variables, it is still possible to see the influence up to 9 ft upstream of the BLI propulsor, as well as at the fuselage up-sweep. The maximum observed displacement was 0.12 inches, and it occurs at approximately

one foot upstream of the BLI propulsor, along the bottom centerline.

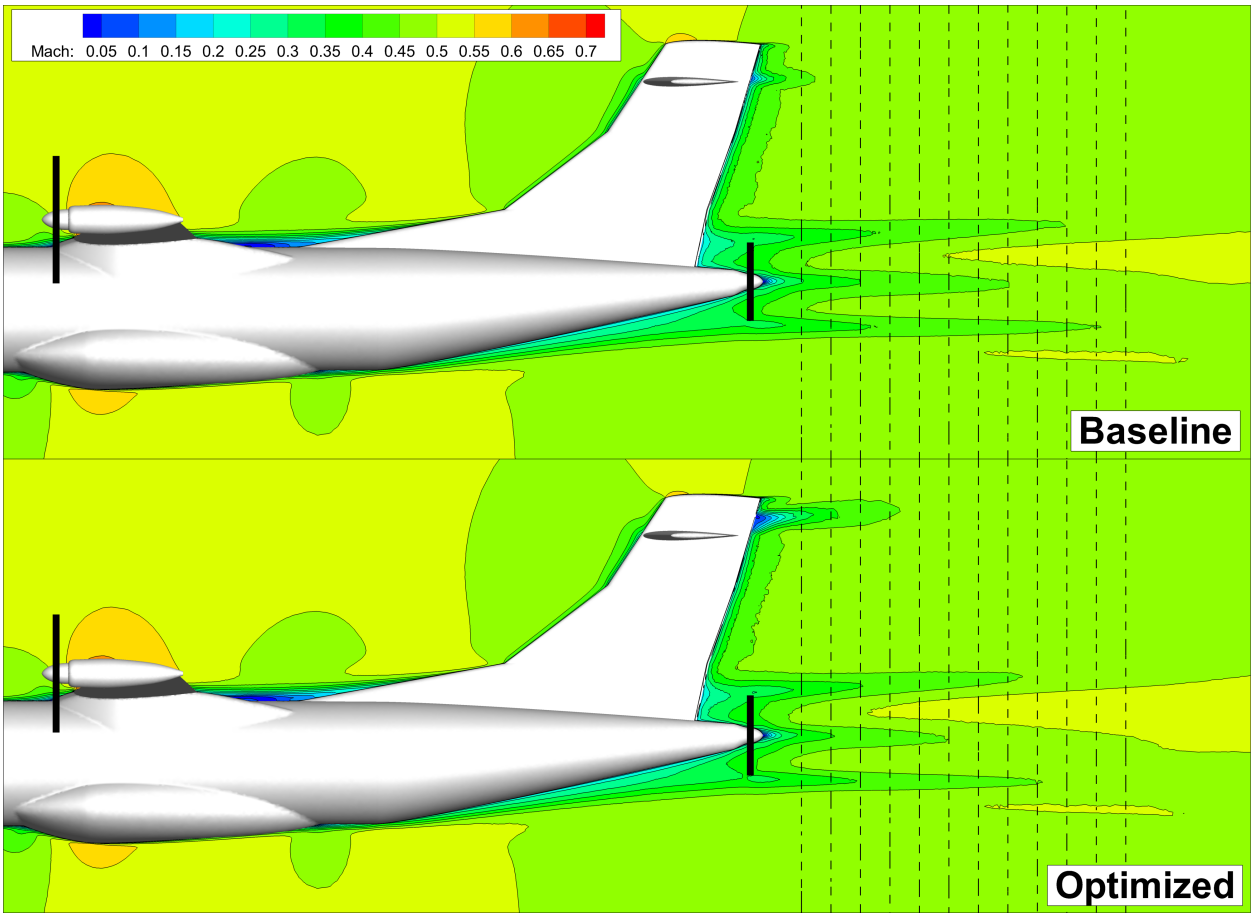

Fig. 8 Mach contours for baseline and optimized PEGASUS concept.

VI. Summary and Future Work

The work presented is an initial effort aimed to expand the design capability within FUN3D, and to allow a better understanding of the design space associated with new advanced concepts which leverage strong aero-propulsive interactions to improve efficiency. The implemented discrete adjoint approach allows us to significantly reduce the computational time and resources required to perform efficient gradient-based design with RANS CFD analysis.

The sensitivity derivatives were verified by the independent complex variable approach. In addition, two academic cases for which general physical behavior is known *a priori* were used to verify that the optimization behaves as expected and in a consistent manner. The optimization of the PEGASUS concept at cruise condition provides an early attempt at the aero-propulsive design of a distributed propulsion concept. This work optimized thrust and power splits for two different propulsor positions based on a simplified representation using actuator disks. Constraints were imposed on the actuator design variables to restrict the design to physically viable design solutions in the absence of more detailed propulsion modeling.

Although not thoroughly exercised with the PEGASUS concept, the current formulation allows for far more flexible design studies applicable to concepts with more heavily distributed propulsion systems, such as NASA's X-57 demonstrator. The available sensitivities allow not only sizing and scaling of the propulsor, but also optimization of position and thrust vector at any point along the flight (e.g., take-off, climb, and cruise). This capability may also be applicable to small UAVs, particularly if the current implementation of performance constraints is extended to include moment constraints in addition to the current net force constraints.

Future work will aim to address shortcomings of the current approach, which include the use of uniform loading on

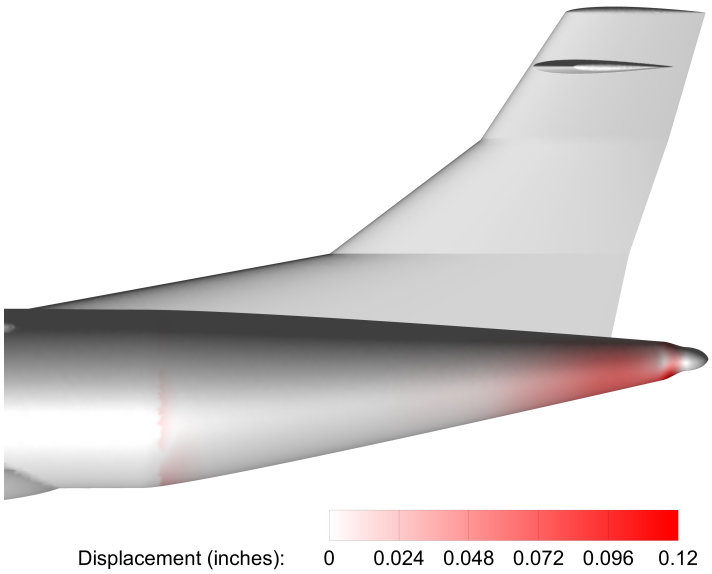

Fig. 9 Magnitude of OML displacement for optimized PEGASUS aft fuselage region.

the actuator disk, the absence of swirl effects due to the torque imparted on the flow, and the requirement to impose an additional flow distortion [17] constraint for BLI propulsors. The ability to impose a flow distortion constraint will be extended to actuator disks from earlier work performed by the authors in Ref. 18.

We currently optimize total flow power by assuming that all propulsors scale similarly with respect to their power requirements. We would like to incorporate more detailed propulsive models and corresponding sensitivities to allow us to optimize with respect to a more appropriate goodness metric based on either fuel and/or energy consumption, and which also account for the scaling effects of such propulsors. The formulation will need to be sufficiently general to allow application of different types of propulsion technologies.

Lastly, the work establishes a framework for the extension of new optimization objectives based on actuator model design variables. These new objectives could reside in disciplinary fields outside aerodynamics and propulsion, such as acoustics, and would allow for a more multidisciplinary and multi-point (e.g., take-off and cruise) design optimization.

Appendices

A. Additional Tables

This Appendix section contains additional tables showing the verification of the design sensitivities through comparison to a complex variable approach. The digits that differ between the adjoint and the corresponding complex sensitivities are shown underlined.

Table A-1 Verification of sensitivities for power objection function

	α	Shape parameter	Ct
Adjoint	1.7820364735938E-10	3.260184448422523E-09	-4.0288274549880E-03
Complex	1.782036515888178E-10	3.260184448323580E-09	-4.028827454987949E-03
	ϕ_1	ϕ_2	ϕ_3
Adjoint	-2.3217836958209E-10	-8.3954778618208E-09	2.3217836958207E-10
Complex	-2.321783695826683E-10	-8.395477861795429E-09	2.321783695826140E-10
	x_0	y_0	z_0
Adjoint	-8.6300948006060E-06	1.8118926610784E-06	5.6189430045981E-07
Complex	-8.630094800551318E-06	1.811892661072672E-06	5.618943004652318E-07
	λ	R_{tip}	
Adjoint	-2.4673258530843E-04	-4.7924470838378E-03	
Complex	-2.467325853084286E-04	-4.792447083837747E-03	

Table A-2 Verification of sensitivities for force constraint along x-direction

	α	Shape parameter	Ct
Adjoint	1.7453157980866E-03	3.810474256823918E-05	-1.5408154619560E-01
Complex	1.745315798118868E-03	3.810474256418334E-05	-1.540815461955578E-01
	ϕ_1	ϕ_2	ϕ_3
Adjoint	7.4308163906763E-12	-1.1540318451858E-10	-7.4308163906016E-12
Complex	7.430816387150731E-12	-1.154031757591400E-10	-7.430816387145824E-12
	x_0	y_0	z_0
Adjoint	3.2680886125103E-05	8.4633134376574E-05	-5.7515075826310E-08
Complex	3.268088612161496E-05	8.463313437351027E-05	-5.751507412292331E-08
	λ	R_{tip}	
Adjoint	-9.4362289440051E-03	-9.4442733131395E-02	
Complex	-9.436228944002726E-03	-9.444273313137077E-02	

Table A-3 Verification of sensitivities for force constraint along z-direction

	α	Shape parameter	Ct
Adjoint	9.6798585064730E-05	2.055672969376386E-04	2.3101112836718E-06
Complex	9.679858505703802E-05	2.055672969382991E-04	2.310111275718748E-06
	ϕ_1	ϕ_2	ϕ_3
Adjoint	-9.9675934863532E-11	1.0329032568974E-04	9.9675934863533E-11
Complex	-9.967593486275961E-11	1.032903256897417E-04	9.967593486275469E-11
	x_0	y_0	z_0
Adjoint	1.0020177572633E-07	-2.3133389905393E-07	3.5353790041249E-05
Complex	1.002017762408483E-07	-2.313338982719911E-07	3.535379004084054E-05
	λ	R_{tip}	
Adjoint	1.4147533885199E-07	1.1464002947891E-06	
Complex	1.414753383649121E-07	1.146400289845558E-06	

Acknowledgment

The work presented was supported by the Advanced Air Transport Technology (AATT) project at NASA. The authors would also like to thank Nathaniel Blaesser at NASA LaRC for providing the initial design and sizing of the wing mounted and fuselage mounted rotors for the PEGASUS concept, Mike A. Park at NASA LaRC for early discussions regarding strategies for the calculation of the flow power objective within FUN3D, and Li Wang at the National Institute of Aerospace for valuable discussions associated with formulation of the optimization problem.

References

[1] Welstead, J. R., and Felder, J. L., "Conceptual Design of a Single-Aisle Turboelectric Commercial Transport with Fuselage Boundary Layer Ingestion," *54th AIAA Aerospace Sciences Meeting*, AIAA Paper 2016-1027, 2016.

[2] Borer, N. K., Patterson, M. D., Viken, J. K., Moore, M. D., Clarke, S., Redifer, M. E., Christie, R. J., Stoll, A. M., Dubois, A., Bevirt, J., Gibson, A. R., Foster, T. J., and Osterkamp, P. G., "Design and Performance of the NASA SCEPTOR Distributed Electric Propulsion Flight Demonstrator," *16th AIAA Aviation Technology, Integration, and Operations Conference*, AIAA Paper 2016-3920, 2016.

[3] Antcliff, K. R., and Capristan, F. M., "Conceptual Design of the Parallel Electric-Gas Architecture with Synergistic Utilization Scheme (PEGASUS) Concept," *18th AIAA/ISSMO Multidisciplinary Analysis and Optimization Conference*, AIAA Paper 2017-4001, 2017.

[4] Gray, J. S., Kenway, G. K., Mader, C. A., and Martins, J. R. R. A., "Aeropropulsive Design Optimization of a Turboelectric Boundary Layer Ingestion Propulsion System," *2018 Aviation Technology, Integration, and Operations Conference*, AIAA Paper 2018-3976, 2018.

[5] "FUN3D Resource Website," http://fun3d.larc.nasa.gov, Accessed: November 2018.

[6] Biedron, R. T., Carlson, J.-R., Derlaga, J. M., Gnoffo, P. A., Hammond, D. P., Jones, W. T., Kleb, B., Lee-Rausch, E. M., Nielsen, E. J., Park, M. A., Rumsey, C. L., Thomas, J. L., , and Wood, W. A., "FUN3D Manual 13.4," NASA TM-2018-20096, 2018.

[7] van Leer, B., "Multidisciplinary Optimization Method for Designing Boundary-Layer-Ingesting Inlets," *Journal of Computational Physics*, Vol. 32, 1979, pp. 101–136.

[8] Spalart, P., and Allmaras, S., "A One-Equatlon Turbulence Model for Aerodynamic Flows," *30th AIAA Aerospace Sciences Meeting and Exhibit*, AIAA Paper 92-0439, 1992.

[9] O'Brien, D., "Analysis of Computational Modeling Techniques for Complete Rotorcraft Configurations," Ph.D. thesis, Georgia Institute of Technology, May 2006.

[10] Nielsen, E. J., and Diskin, B., "Discrete Adjoint-Based Design for Unsteady Turbulent Flows on Dynamic Overset Unstructured Grids," *AIAA Journal*, Vol. 51, No. 6, 2013, pp. 1355–1373.

[11] Nielsen, E. J., and Anderson, W. K., "Recent Improvements in Aerodynamic Design Optimization on Unstructured Meshes," *AIAA Journal*, Vol. 40, No. 6, 2002, pp. 1155–1163.

[12] Biedron, R. T., and Thomas, J. L., "Recent Enhancements to the FUN3D Flow Solver for Moving-Mesh Applications," *47th AIAA Aerospace Sciences Meeting including The New Horizons Forum and Aerospace Exposition*, AIAA Paper 2009-1360, 2009.

[13] Moler, C. B., and Lyness, J. N., "Numerical Differentiation of Analytic Functions," *SIAM Journal of Numerical Analysis*, Vol. 4, No. 2, 1967, pp. 202–210.

[14] Squire, W., and Trapp, G., "Using Complex Variables to Estimate Derivatives of Real Functions," *SIAM Review*, Vol. 10, No. 1, 1998, pp. 110–112.

[15] Anderson, W., Newman, J., Whitfield, D., and Nielsen, E. J., "Sensitivity Analysis for Navier-Stokes Equations on Unstructured Meshes Using Complex Variables," *AIAA Journal*, Vol. 39, No. 1, 2001, pp. 56–63.

[16] Samareh, J. A., "Aerodynamic Shape Optimization based on free-form deformation," AIAA Paper No. 2004-4630, 2004.

[17] "Gas Turbine Engine Inlet Flow Distortion," SAE ARP-1420, Society of Automotive Engineers, March 1978.

[18] Ordaz, I., Rallabhandi, S. K., Nielsen, E. J., and Diskin, B., "Mitigation of Engine Inlet Distortion through Adjoint-Based Design," *35th AIAA Applied Aerodynamics Conference*, AIAA Paper 2017-3410, 2017.